ORIGINAL ARTICLE

lajss.org© Latin American Journal of Solids and Structures

www.lajss.org

Energy absorption and indentation resistance of re-entrant arched honeycomb reinforced by circular ribs

Shilong Wang[a]*, Yang Liu[a], Haiying Bao[a], Zhilai Huang[b]

[a]School of Civil Engineering and Architecture, Anhui University of Technology, Ma'anshan, Anhui 243002, PR China. E-mails: wshilong2012@163.com, 2738721212@qq.com, baohaiying@ahut.edu.cn

[b]School of Mechanical Engineering, Anhui University of Technology, Ma'anshan, Anhui 243002, PR China. E-mails: zhilai_huang@foxmail.com

* Corresponding author

https://doi.org/10.1590/1679-7825/e8489

Abstract

To enhance the mechanical properties while keeping controlled auxetic performance, a novel circular reinforced re-entrant arched honeycomb (CRRAH) structure is developed. CRRAH specimens were additively manufactured, and quasi-static compression tests were conducted to evaluate their performance. Results demonstrate that superior mechanical performance is presented by comparing to the conventional re-entrant arched honeycomb structures, including a remarkable 208% increase in specific energy absorption (SEA). The finite element model, validated against experimental results, was further used to explore the deformation mechanism and auxetic performance of CRRAH structures with varying thickness ratios (γ). Results indicated that integrating circular rib within the re-entrant cells effectively restricts the continuous rotational stretching of inclined ligaments, resulting in a two-stage collapse process. This significantly enhances the deformation stability and energy absorption capacity. Moreover, adjusting the thickness ratio γ shifts the deformation mode from localized shear band formation to uniform global deformation with slight lateral expansion. Moreover, the dependence of deformation and the indentation resistance performance on thickness ratio were explored and the underlying mechanism was revealed. These findings provide valuable insights into the design of advanced re-entrant honeycomb structures, combining improved crashworthiness with controlled auxetic effects.

Keywords

Re-entrant honeycomb, auxetic behavior, energy absorption, deformation mechanism, indentation resistance

Graphical Abstract

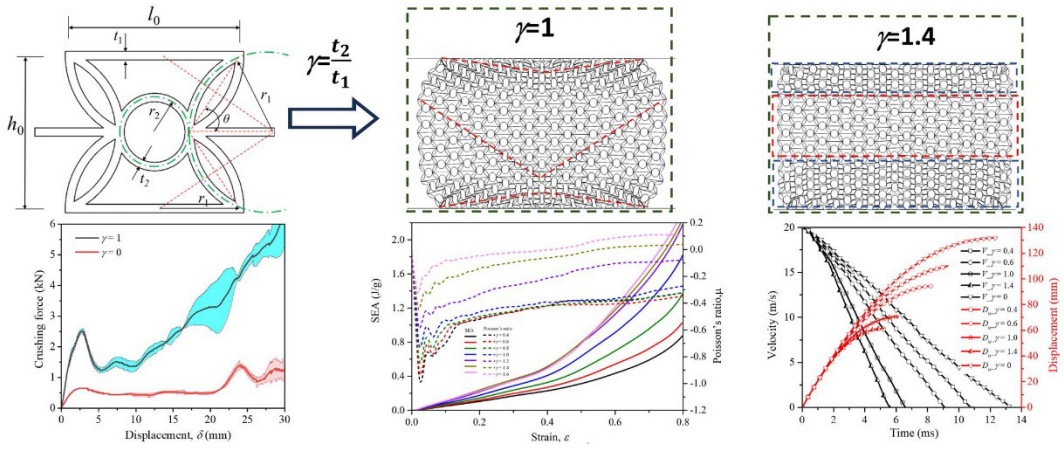

Received December 11, 2024. In revised form January 23, 2025. Accepted January 24, 2025. Available online January 28, 2025.
https://doi.org/10.1590/1679-7825/e8489

1 INTRODUCTION

The honeycomb structure, a typical multi-cellular structure with periodically arranged in-plane cells, exhibits numerous advantageous physical and mechanical properties, including light weight, high specific strength, and excellent energy absorption. Due to these characteristics, it is widely utilized as an energy-absorbing structure in crashworthiness applications, such as automotive, aerospace, packaging industries and maritime engineering, generally serving as core components in sandwich structures (Zhang and Xu, 2022; Li et al., 2024; Palomba et al., 2022; Nunes and Silva, 2016). Especially, the abundant pore spaces within cells enables them to undergo significant plastic deformation while maintaining a relatively long low plateau stress. This property allows them to exhibit excellent impact resistance, continuing to absorb energy effectively until they collapse into a more stable state or eventually fracture (Chen et al., 2019). With its simple configuration and strong designability, honeycomb structures go beyond the traditional regular hexagonal cell. Various cell shapes and in-plane topological arrangements have been proposed. These innovative honeycomb structures retain the mechanical properties of traditional honeycombs while offering tailored performance, such as enhanced load-bearing capacity, improved energy absorption, and negative Poisson's ratio (NPR) effects (Arnob et al., 2023; Xiao et al., 2019; Baran and Öztürk, 2020; Zhang et al., 2020), effectively meeting the expected requirements for various engineering applications

The advancement of additive manufacturing techniques has significantly enhanced the ability to fabricate structures with desirable cell topologies, offering great design freedom and allowing for unrestricted complexity. Among various additive manufacturing methods, selective laser sintering is commonly used to fabricate honeycomb structures using base materials such as metals (Xiao et al., 2019; Zhao et al., 2024) or polyamide (Azam et al., 2023). On the other hand, fused deposition modeling (FDM) is widely adopted to create honeycomb structures with different thermoplastic matrices (Garbatov et al., 2024; Isaac and Duddeck, 2022). Specifically, ABS (acrylonitrile butadiene styrene) and PLA (polylactic acid) are two of the most widely used thermoplastic materials for the FDM process due to their advantages, including a well-balanced overall performance, easy availability of raw materials, low cost, and their recyclable and sustainable nature (Olivera et al., 2016; Joseph et al., 2023). Among various meso-structural topologies, honeycomb structures with NPR behavior have garnered significant attention for their unique mechanical properties. For instance, it has been reported that honeycomb structures made from ABS demonstrate excellent ductility and a desirable NPR effect under large deformations (Hu et al., 2019). NPR honeycombs, a unique type of honeycomb structure, exhibit deformation patterns opposite to those of conventional honeycombs under uniaxial tensile or compressive loads. Due to the re-entrant angles within the structure, the honeycomb expands when under tensile loading (as the re-entrant angles decrease) and contracts when compressed (as the re-entrant angles increase) (Shen et al., 2021). Except to the lightweight, high specific strength, high specific stiffness, and energy absorption capabilities typical of traditional honeycombs, NPR honeycombs also demonstrate high compressive strength and distinctive resistance to shear and indentation (Giménez-Ribes et al., 2022; Pang et al., 2024; Wang et al., 2019; Bohara et al., 2023; Li et al., 2020), making them highly suitable for a range of applications. Although re-entrant honeycombs exhibit a range of enhanced physical and mechanical properties, the high porosity weakens the sufficient strength and stiffness of re-entrant honeycombs compared to solid materials. In many cases, the benefits of the NPR do not fully compensate for the mechanical limitations introduced by the porous structure, which can reduce the advantages of NPR effect, particularly in energy absorption and cushioning applications (Chen et al., 2024; Ren et al., 2018). Thus, enhancing the crushing performance of NPR honeycombs without significantly diminishing their auxetic performance becomes an important design approach.

The mechanical properties of honeycomb structures depend not only on the base material but also on the topology and arrangement of the cells (Qi et al., 2021). Thus, by altering cell configurations and arrangements, various types of re-entrant honeycomb structures have been proposed. Considering the stress concentration raised in the corners of re-entrant edges within straight cell walled re-entrant honeycombs, Guo et al. (2023) studied the in-plane crushing behavior of elliptical anti-chiral honeycomb structures, where regular straight cell walls were replaced with elliptical ones. Results indicated that such adaptation enhanced the crushing strength of the honeycomb. On the basis of traditional rhombus honeycomb, Feng et al. (2021) designed two kinds of honeycombs with curved cell walls, significantly improving mechanical performance. Focusing on unit cell design, Körner and Liebold-Ribeiro (2014) used eigenmode analysis to identify auxetic re-entrant structures with sinusoidal or chiral re-entrant cells, providing valuable insights into the design and analysis of novel materials with auxetic properties. Additionally, sinusoidal honeycombs with circular nodes were developed by introducing thin-walled circular rings at the nodes, resulting in improved energy absorption compared to conventional sinusoidal honeycombs under various impact loads (Feng et al., 2023). To further enhance energy absorption, Qi et al. (2020) proposed a re-entrant circular honeycomb structure, substituting the conventional inclined cell walls with double circular arc walls, leading to a varied Poisson's ratio and superior energy absorption compared to conventional re-entrant honeycombs. By combining the hexagonal honeycomb and auxetic structure, a new type of

hybrid re-entrant honeycomb termed as AuxHex structure was constructed (Xu et al., 2019), and they exhibited enhanced in-plane compressive strength and convertible Poisson's ratios depending on the ligament lengths. Similar strategy was adopted by Zhang et al. (2022a, b) to generate a vertical strut and hexagon combined auxetic structure. Results indicated that the hybrid auxetic structure possessed higher crushing strength and energy absorption capacity than re-entrant structures. Ni et al. (2024) considered an enhanced re-entrant honeycomb by incorporating re-entrant and chiral honeycomb, and the excellent auxetic behavior and specific energy absorption were presented compared to the conventional honeycomb.

Apart from the design of cell configuration and arrangements, introducing additional components into the matrix cells is also an effective way to enhance the crushing performance of re-entrant honeycomb structures (Chen and Fu, 2018; Tatlıer et al., 2021; Zou et al., 2023). By embedding the rhombic configuration into normal re-entrant hexagonal cells, Fu et al. (2017) developed a novel auxetic honeycomb. Results indicated that the Young's modulus and the buckling strength of this new auxetic honeycomb were effectively improved while maintaining the auxetic performance. Wang et al. (2024a) treated the rhombic structure as reinforced structure inside the star-shaped structure and designed a hybrid star-rhombus honeycomb. With different strategies of filling the rhombic structure inside the star-shaped honeycomb, the programmable mechanical responses were expected to achieved. Additionally, increasing the local buckling resistance and deformation stability of re-entrant walls is also an available method to improve the mechanical properties, especially the stiffness. This can be achieved by adding new inclined walls (Baran and Öztürk, 2020), incorporating augmented vertical strut (Li et al., 2019), adding wedge parts (Zhang et al., 2020) and inserting stretch-dominated truss elements in the nodes (Jafari Nedoushan et al., 2023). Considering the eroded negative Poisson's ratio properties when enhancing the stiffness, strength or energy absorption capacity, Zhu et al. (2024) introduced the elliptical annular structure into conventional re-entrant honeycomb and results demonstrated the elliptical annular re-entrant honeycomb featured an improved energy absorption performance while keeping a strong auxetic effect.

Compared to re-entrant honeycomb structures with straight cell walls, arc-shaped re-entrant honeycombs demonstrate improved energy absorption performance (Feng et al., 2021). This is primarily due to the use of curved re-entrant edges instead of traditional straight edges, which enables the formation of more plastic hinges during the crushing process. Additionally, the arched cell walls occupy a larger space, enhancing the local buckling and collapse strength of the individual cells (Qi et al., 2020). Combing the design concept of arch cell wall replacement and enhanced structure embedding, it would be promising to design a novel re-entrant honeycomb structure with promising mechanical properties, in terms of crushing strength, energy absorption capacity and auxetic performance. In this study, the design approach of incorporating circular reinforcement ribs within arc-shaped re-entrant honeycomb structures is explored and a novel circular reinforced re-entrant arched honeycomb (CRRAH) structure with strengthened mechanical performance is proposed. CRRAH specimens were fabricated using 3D printing technology, and quasi-static in-plane compression tests were conducted to comparatively analyze the deformation failure modes and macroscopic mechanical properties after introducing circular reinforced ribs. Additionally, a meso-scale finite element model was used to examine the influence of meso-structural parameters, such as cell size and wall thickness of reinforced components on the deformation patterns, auxetic effects, and energy absorption performance. Finally, the impact of varying the ratio of circular reinforced rib thickness to honeycomb wall thickness on impact resistance and penetration performance was analyzed.

2 MATERIALS AND METHODS

2.1 Geometrical configuration design

The construction of circular reinforced re-entrant arched honeycomb (CRRAH) structure is on the base of geometrical configuration of re-entrant circular honeycomb. The geometrical configuration of CRRAH unit is described as follows: By drawing the perpendicular bisector of the oblique edges of conventional re-entrant cell, the two intersection points on the horizontal edges could be obtained. Taking the intersection points as the center and the distance from the intersection point to the vertex as the radius, the intersection arch segments are determined and are used to replace the initially oblique edges, as shown in Figure 1(a). Similar process is repeated for the rest oblique edges. Then, a circle is introduced at the right center of the re-entrant circular cell to enhance the crushing stability. The designed configuration of the unit cell is controlled by the parameters of cell width l_0, vertical height h_0, radius of inclined arch r_1, radius of enhanced circle r_2, thickness of enhanced circle t_2, thickness of the rest cell edges t_1, and the out-of-plane height b. The geometric and assembled compatibility of the developed cell unit require that $2r_1$ should be large than h_0 and less than l_0, as shown in Figure 1(b). A parameter γ, defined as the ratio of thickness of cell edge t_2 to the thickness of enhanced circle t_2 is adopted to quantitatively describe the proportion of the enhanced element within a cell, as shown in Figure 1(c-e).

$$r_1 = \frac{h_0}{2\sin 2\theta} \tag{1}$$

$$r_2 = \frac{l_0}{2} - \frac{h_0}{4}\cot\theta \tag{2}$$

$$\theta = \arccos\left(\sqrt{\frac{l_0}{2r_1} - \frac{r_2}{r_1}}\right) \tag{3}$$

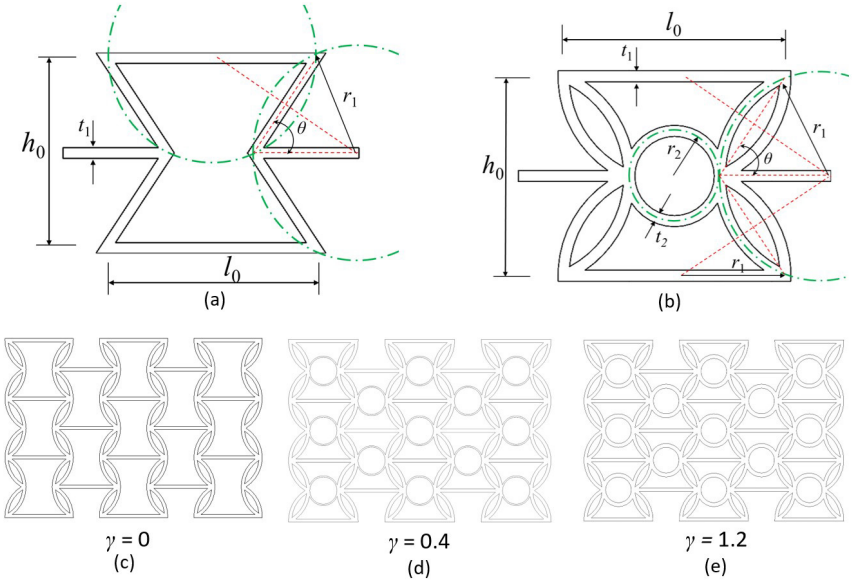

Figure 1: Conventional re-entrant cell (a), re-entrant cell with circular reinforced rib (b), CRRAH structures with γ = 0 (c), γ = 0.4 (d) and γ = 1.2 (e).

2.2 Preparation of additively manufactured specimen

The CRRAHs are additively manufactured via fused deposition modeling (FDM) technology on a 3D printing machine of HORI X400 Plus. The available fabricating dimension is 400×250×230 mm^3, and the diameter of extrusion nozzle is 0.4 mm with the printing accuracy of 0.01mm in XY plane and 0.05 in Z direction. The printing process of CRRAHs is shown in Figure 2(a). The adopted base material is acrylonitrile butadiene styrene (ABS) plastic which has considerable ductility (Ran and Yang 2020). Additionally, ABS stands out as a recyclable thermoplastic material (Deshmukh et al., 2024). This characteristic, combined with its well-balanced mechanical properties and cost-effectiveness, makes ABS a promising candidate for applications requiring sustainability and performance. During printing, the temperatures of nozzle and supported bed were set as 240°and 70°, respectively. The printing speed is adjusted to 40 mm/s with a slice height of 0.1 mm to ensure the dimensional accuracy. The manufactured CRRAHs have the same configuration of l=20mm, h=18mm, r_1=10.1mm, r_2=4.5mm, b=20mm, L=78mm, H=55mm, t_1=t_2=1mm. A printed ABS CRRAH specimen is shown in Figure 2(b). Additionally, three specimens were fabricated for each of the configuration for duplicate tests. The standard tensile specimens were also fabricated to determine the material properties with the same printing parameters.

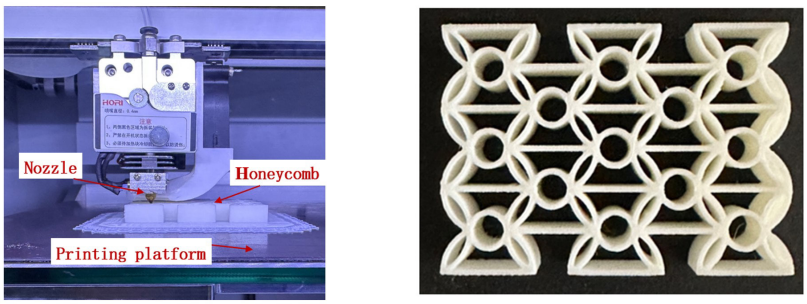

(a) (b)

Figure 2: The 3D printing process of fabricating honeycomb (a) and the printed CRRAH (b).

2.3 Tensile and in-plane compression tests

In order to obtain the mechanical properties of 3D printed ABS materials, tensile specimens were prepared in accordance to GB/T 1040.1–2018 (P.R. China, Standardization Administration, 2018). Uniaxial tensile tests were performed on them. The engineering stress-strain curve was obtained after dealing with the experimental data as shown in Figure 3(c), and the basic mechanical properties of ABS are listed in Table 1. The aluminum alloy material, whose mechanical properties were determined in our previous study (Wang et al., 2021) and summarized in Table 1, is further considered as the base material for the developed honeycomb structure analyzed in the following sections. The engineering stress-strain data is then converted to the true stress-strain relation that is acquired in simulations (as shown in Figure 3(c)), with the formula in Eqs. (4-5).

$$\sigma_T = \sigma_N \left(1+\varepsilon_N\right) \tag{4}$$

$$\varepsilon_T = \ln\left(1+\varepsilon_N\right) \tag{5}$$

As shown in Table 1, ABS exhibits relatively low tensile strength and modulus compared to aluminum alloy. Given that the primary goal of developing novel honeycomb structure is to enhance crashworthiness, the compressive performance becomes particularly crucial in protective applications, where tensile properties are less critical. Therefore, this study focuses on the compressive behavior of ABS honeycomb structures to evaluate their potential in such applications, where compressive strength, energy absorption, and structural stability are key performance indicators (Isaac and Duddeck, 2022). Additionally, as a commonly used additive material, ABS contributes to the development of lightweight structures with desirable mechanical properties in an efficient and cost-effective manner.

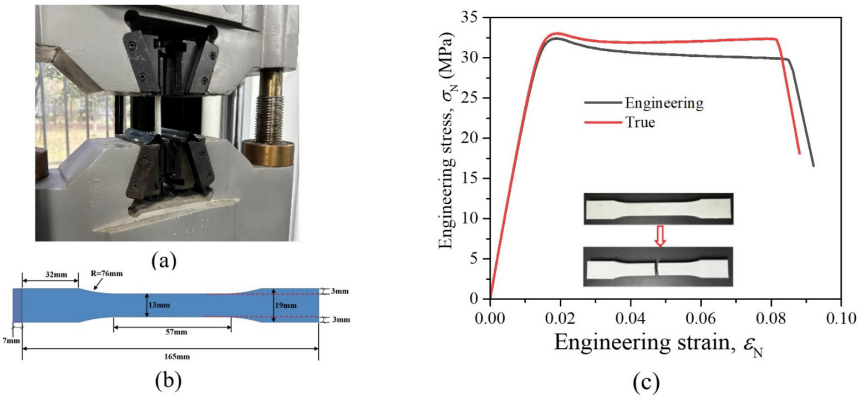

Figure 3: The test setup for tensile test (a), the dimension of tensile specimen (b) and the corresponding tensile stress-strain curve of ABS material (c).

Table 1 Material parameters for the ABS and aluminum.

Material	Modulus of elasticity	Yield strength	Tensile strength	Density
	(MPa)	(MPa)	(MPa)	(g/cm^3)
ABS	2400	31.4	30.8	1.0
Aluminum	47300	193.1	213.7	2.8

A WAW-300D electro-hydraulic servo pressure tester with a loading capacity of 300 kN was used to perform quasi-static compression tests on CRRAHs as shown in Figure 4. Before loading, the honeycomb specimen was placed vertically between the upper and lower circular platens without fixtures. Among them, the lower platen was totally fixed whereas the upper platen was applied a vertical downward displacement load during compression, maintaining a constant loading rate of 3.3 mm/min. The reaction force applied to the upper platen was recorded by a sensor at the loading end, and the data were transferred to a connected computer, where the displacement and load data were obtained through software processing. At the same time, a high-resolution camera was used to record the deformation pattern of the specimen during compression. The same experiment was repeated three times in order to minimize the effect of errors in the experimental results.

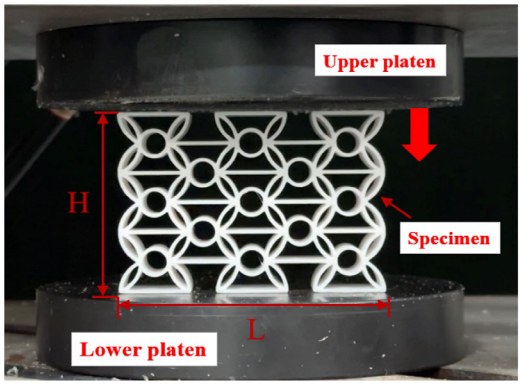

Figure 4: Quasi-static compression test setup for CRRAHs.

2.4 Numerical modeling

Numerical simulation using ABAQUS/EXPLICIT was also carried out to analyze the dependence of the mechanical responses of CRRAH structure on the designed topology. Figure 5 shows a finite element model whose configuration and dimensions are consistent with that of the printed specimen. Considering the complexity of the topological features of the CRRAH structure, the cell walls are modeled using the four- node linear shell elements with reduced integration and finite mem- brane strains (S4R). After the mesh sensitivity analysis, a mesh size of 0.4 mm is determined to be optimal, which achieves a good balance between numerical stability, accuracy and computational efficiency. The numerical simulation is consistent with the experimental loading conditions, where the honeycomb specimen is placed between two rigid plates. The loading plate only moves downward along the Y-axis at a uniform speed of 5m/s, while the support plate is completely fixed. A general contact is used to define all possible contacts during the calculation, and the friction coefficient is set to 0.3.

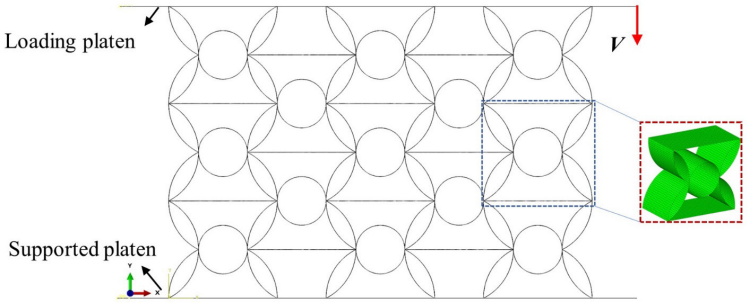

Figure 5: Finite element model of CRRAH.

3 RESULTS AND DISCUSSION

3.1 Comparison of in-plane crushing behavior of CRRAH with and without circular reinforced ribs

The in-plane crushing responses of CRRAHs with $\gamma = 0$ and $\gamma = 1$ is compared, as shown in Figure 6(a). The force-displacement curves for the same configurations could coincide well with each other, highlighting the excellent performance consistency of printed specimens. Basically, the crushing process of CRRAH of $\gamma = 1$ can be divided into three stages. In the first stage, structure behaves linearly as the compression displacement increases. With the continued increase of compression distance, buckling of local cells is initiated, accompanying a force drop after the peak value on the load-displacement curves. In the collapse stage, cells progressively buckle and collapse to a long compression distance until all collapsed cells contact with each other. Then, further compression leads honeycomb structure enter into compacted stage, in which the crushing force increase rapidly with displacement. Different from the almost unchanged plateau force appeared in conventional honeycomb structures (Qi et al., 2021), CRRAH of $\gamma = 1$ exhibits a gradually increasing plateau stage due to the introduction of enhanced elements, indicating the improved crushing performance. For CRRAH without circular reinforced ribs, the crushing process also experiences three stages. Different from CRRAH of $\gamma = 1$, the crushing force of CRRAH of $\gamma = 0$ at the plateau stage can maintain a nearly constant for a wide range of crushing displacement. Globally, the crushing strength is much lower than that of CRRAH of $\gamma = 1$.

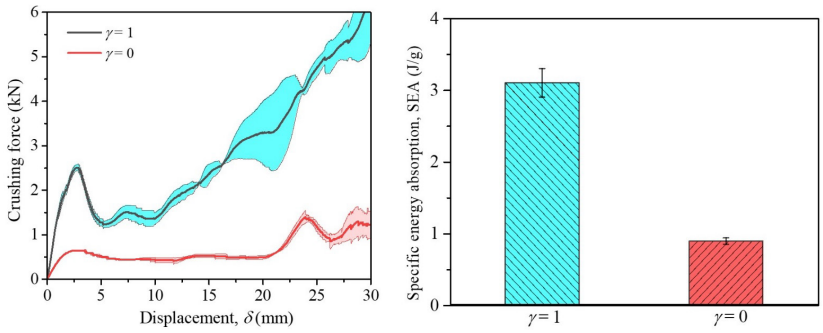

(a) (b)

Figure 6: Comparison of the crushing force-displacement curves of CRRAH of $\gamma = 0$ and $\gamma = 1$ (a), and specific energy absorption (SEA) (b).

To evaluate the energy absorption property of honeycomb structures, the specific energy absorption (SEA) index is adopted, which is defined as the total energy absorbed before densification to the mass

$$SEA = \frac{\int_0^{\delta_d} F(x)dx}{M} \tag{6}$$

Where M is the mass of structure, $F(x)$ is the instantaneous crushing force, and δ_d is the effective crushing stroke before densification, which can be determined based on the energy absorption efficiency curve (Wang et al., 2021). The results show that CRRAH of $\gamma = 1$ achieves significantly better energy absorption performance than CRRAH of $\gamma = 0$, with a 208% increase in SEA compared to RECH under identical design parameters, as shown in Figure 6(b).

A sequence of deformation patterns of CRRAHs is shown in Figure 7. Initially, both structures deform elastically and no obvious deformation is observed, as shown at a loading displacement of $\delta = 2.5$ mm. With continued loading, buckling of local cells occurs and the evident deformation begins to appear in the specimens. At this stage, the curved cell walls of both structures collapse in the form of bending and rotating at the junctions with the horizontal walls, forming a diagonally X shear band, as illustrated in the deformation patterns under at a loading displacement of $\delta = 10$mm. Comparingly, the notable difference is that in CRRAH structure with $\gamma = 1$, the embedded circular ribs partly hinder the rotation of the curved cell walls, causing the enhanced elements to deform into elongated arcs. The central enhanced elements within the CRRAH of $\gamma = 1$ exhibit the most pronounced deformation, and finally the embedded enhanced member walls contact with the horizontal linked cell walls before the totally collapse of local regions. This deformation pattern thus provides additional longitudinal support to the cell walls and also induces more cell walls more cell elements to participate in plastic deformation for energy dissipation.

As the loading progresses and reaches a displacement of δ=18 mm, the collapsed cells along the central row tightly stack together for CRRAH of $\gamma = 1$ whereas the deformation bands remain loose state and can be further compressed in these regions of CRRAH of $\gamma = 1$. The rotation deformation of inclined edges results in lateral contraction towards the center. This contraction causes cell elements in the peripheral regions to move toward the center, creating a characteristic NPR effect. However, due to the obstructive effect of the circular reinforced ribs, the NPR effect is less pronounced in the CRRAH than in the re-entrant arched honeycomb. When the compression distance is further increased, all of the collapsed curved walls would come into contact and stack tightly together with each other, as shown in Figure 7 under $\delta = 25$mm. It is worthy noticed that for CRRAH structure of $\gamma = 1$, the supporting effect and the collaborative rotation deformation of the circular reinforced ribs make the cell walls being fully collapsed, which is conducive to improve the energy absorption capacity.

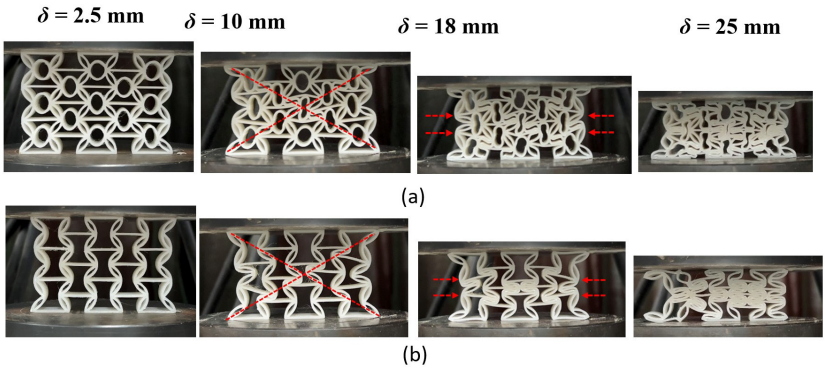

(a)

(b)

Figure 7: Deformation patterns of CRRAHs with $\gamma = 1$ (a) and $\gamma = 0$ (b).

3.2 Validation of finite element model

The accuracy and reliability of the finite element model is verified by comparing the crushing responses and deformation modes against experimental results. As shown in Figure 8(a), the crushing force-displacement curve of simulation can well capture the whole crushing process of CRRAH of γ = 1. Clearly, the numerical simulation is in good agreement with the experimental data, demonstrating the reliability of the simulations based on the described material model. Moreover, as shown in Figure 8(b), comparison of the deformation modes illustrates that the initiation of local cells collapse and the formation of shear bands appear in tests are versatilely reproduced by the numerical simulation, which is further validate to predict the crushing behavior under the in-plane compression.

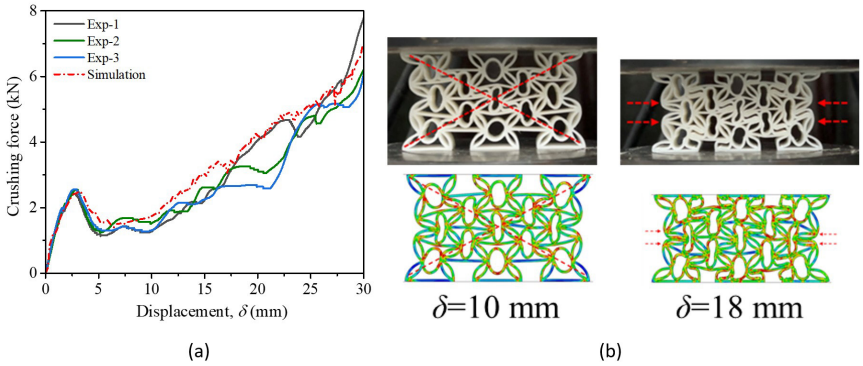

Figure 8: Comparison of the force-displacement curves (a) and deformation patterns (b) of CRRAHs obtained from tests and simulation

3.3 Size effect and deformation mechanism of CRRAH

For honeycomb structure, the deformation mode can also be highly influenced by the boundary conditions and height-to-width ratio of structure (Zheng et al., 2005). Therefore, a large size of CRRAH and RECH structures with 10×11 cells is considered and detail geometrical parameters are: l=20mm, h=18mm, r_1=10.1mm, r_2=4.5mm, b=5mm, t_1=t_2=0.2mm, resulting in a global in-plane area of 273×216 mm^2. Based on the grid convergence analysis, the cell walls are meshed using S4R elements with size of 0.6 mm. To improve computational efficiency in explicit finite element time integration, a loading speed of 5 m/s is chosen, allowing faster simulations while approximating quasi-static conditions. In the process, a mass scaling strategy is applied to ensure kinetic energy remain under 5% of internal energy with minimal inertial effects (Wang et al., 2024b). It also should be pointed that ABS material has the disadvantage of brittle fracture under large deformations (Rezaeian et al., 2022), which can be also captured in Figure 3(c) with a fracture strain of about 0.09. Drawing from practical experience with honeycomb structures in protective engineering, stronger and tougher metal materials are often used as the base material for honeycombs (Wang, 2019). Aluminum alloy, as a widely used tough metal, effectively prevents catastrophic initial instability and deformation, supporting subsequent damage behavior development. Therefore, in the following finite element simulations, aluminum alloy 6063 is selected as the honeycomb base material, and based on our previous studies (Wang et al., 2021), it is assumed to behave as an ideal material with mechanical properties as: Young's modulus of 47.3 GPa, yield stress of 193.1 MPa, density of 2800 kg/m^3 and Poisson's ratio of 0.3, respectively.

The deformation patterns of CRRAH structures with large sizes are shown in Figure 9. At the early crushing stage, the collapse of cells is mainly accumulated at the two ends and the rotation buckling of inclined cell walls generally guides the inward contraction, forming a double "V" shaped shear band. Such deformation mode is quite different from the evident X-shaped mode appear in the small size structures since limited restrictions are exerted on the boundaries. For CRRAH of γ = 1, except for the crushed cells at the ends, a V-shaped band of which vertex initiating from the supported end is also raised in the center region, as shown in Figure 9(a) of ε = 0.25, where the nominal strain ε is defined as ratio of the crushing displacement to the initial height. Due to the enhanced in-plane crushing strength of CRRAH with reinforced elements, the linked adjacent arc cell walls along the load transfer path are more likely to bend and rotate around the reinforced components till collapse. When the compression strain increases to 0.5, both CRRAH with and without reinforced members present similar deformation mode. Obvious contraction on the two free sides is observed and the typical negative Poisson's ratio occurs. Besides, "bulge effect" on the four corners enclosed by the crushed bands at the loading ends and shrinking regions is highlighted. This is mainly caused by the opposite movement and collapse of cells in regions with different loading states. With further increase of displacement, more crushed bands are formed and collapsed cells are generally compacted to densification, accompanying the obvious contraction in lateral direction.

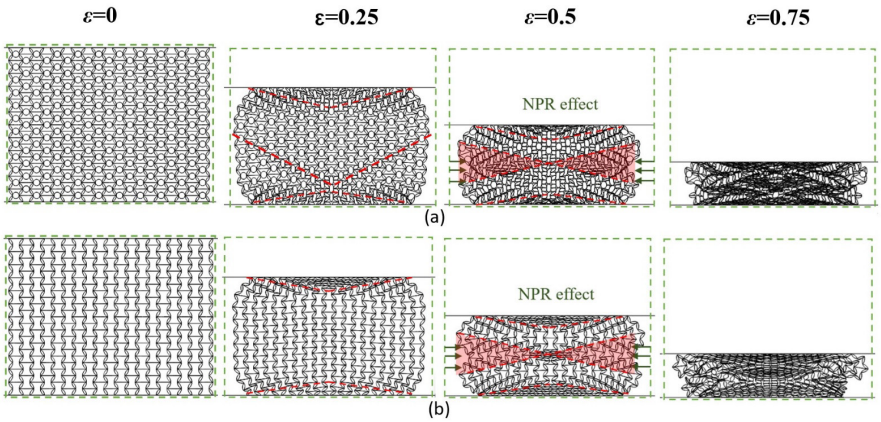

Figure 9: Deformation patterns of CRRAHs with (a) and without (b) reinforced elements.

The stress-strain curves of the two structures are shows in Figure 10(a). Similar to the tendency as presented in experimental result of small size, arched re-entrant honeycomb with large size also exhibits typical three-stage response with a long plateau stress. However, for the large-sized CRRAH of γ = 1, within the plateau stage, a relatively constant force stage is followed by the force hardening rising stage. The two-stage crushing response occur in the CRRAH of γ = 1 are essentially controlled by two deformation mechanisms at the crushing process. During compression, the buckling and collapse of the inclined arched segments prior to the failure of reinforced components. In the first plateau stage, severe deformations mainly occur within the inclined cell edges and the types of deformation patterns experience by unit cells in different regions are classified in Figure 11. The crushed band is early formed at the loading ends and cells in these sites would fail with rotation of diagonal arch segments (as marked of ① in Figure 11), finally resulting the V-shaped crushed bands at the two ends. In the central portion, stress is uniformly and symmetrically exerted on the cells and the adjacent arch edges rotates oppositely with the reinforced component being compressed into dumbbell shapes (as marked of ②). In the region ③, in which the crushed bands with different orientations gather, cells suffer complex loading state caused by the uncoordinated collapse and rotation of the surroundings. While in the free boundary site close to the loading ends (as marked of ④), the adjacent layers of cells tend to contract inward, which leads to the lateral inverse loading case. Thus, the cells in these sites are squeezed outward, forming the bulge phenomena. After the inclined edges collapse into the stable states, further compression would induce the crushing of the reinforced components and the densification of crushed arch edges, leading to the second plateau stage on the stress-strain curve of CRRAH of γ = 1. This sequential mechanism contributes to a more gradual energy absorption, where the structure's resilience increases as the circular reinforcements bear the progressive load.

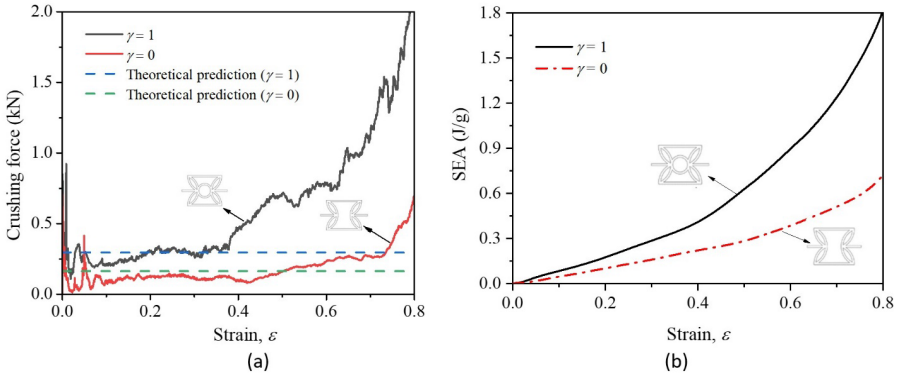

Figure 10: The crushing stress-strain curves (a) and SEA-strain curves (b) of CRRAHs with γ = 1 and γ = 0.

The comparison of the energy absorption capacity of CRRAHs with and without reinforced components is shown in Figure 10(b). It indicates that during the whole crushing process, CRRAH of γ = 1 always exhibits higher energy absorption capacity than that of RECH. Additionally, the difference of SEA between the two types of structures enlarges with increase of global axial strain. This can be explained as the reason that in the later crushing stage, the collapse deformation of the reinforced components gradually plays a dominant role in the dissipation of energy. At an axial strain of 0.8, the SEA of CRRAH with reinforced elements is up to 152% higher than that of arched re-entrant honeycomb. Overall, the reinforced component-enhanced design provides an effective strategy to improve the energy absorption property of re-entrant honeycombs.

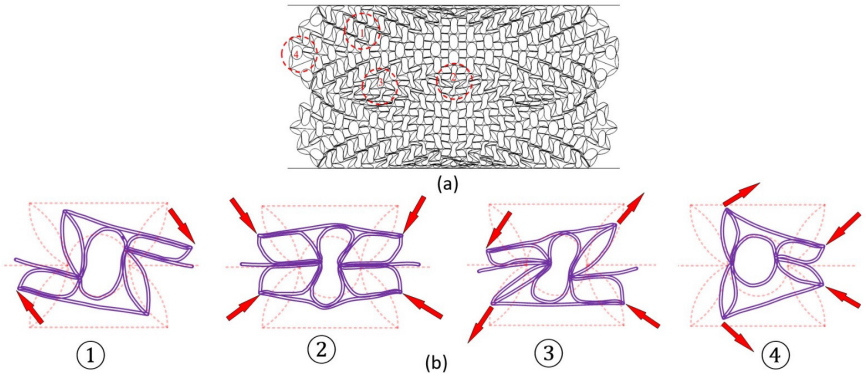

Figure 11: Types of deformation modes experienced by unit cells in different regions.

Further, the representative unit (as shown in Figure 12(a)) is analyzed to theoretically evaluate the crushing strength of CRRAH. Based on the observed deformation pattern of a typical representative unit ②, it is assumed that during the collapse process, the the eight arc segments in the inclined walls deform by forming plastic hinges around the connected joints. Simultaneously, the central circular wall is divided into eight arc segments by forming eight hinges, as shown in representative unit of Figure 12(b). During this process, the arc ABC wall bends continuously around joints A and C until it fully contacts both the connected horizontal wall and the reinforced circular wall, reaching the densification state. Throughout this deformation, the middle portion of the arc ABC wall maintains a nearly constant curvature with negligible deformation. Similarly, the circular arc DE wall bends around joint E until it flattens, while the arc CD wall rotates around joint C until it comes into tight contact with the adjacent collapsed arc wall. Hence, as shown in Figure 12(c) the plastic angles for the three types of arc walls can be approximately expressed as

$$\Delta\varphi_1 = \theta, \Delta\varphi_2 = \frac{\pi}{2} - \frac{3\pi}{8} = \frac{\pi}{8}, \Delta\varphi_2 = \pi - \frac{3\pi}{8} = \frac{5\pi}{8} \tag{7}$$

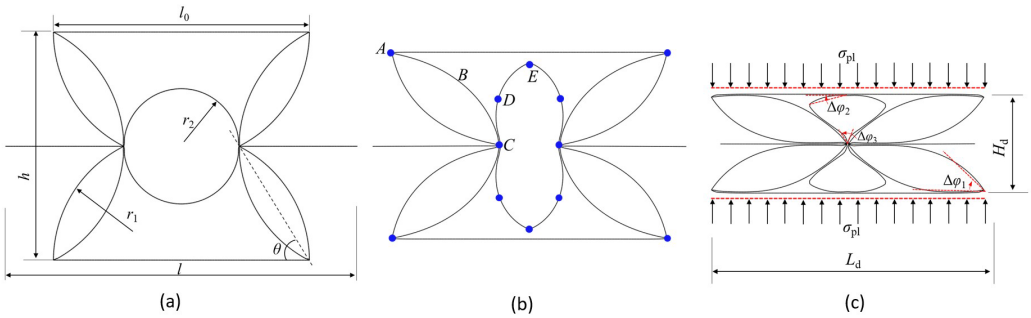

Figure 12: Collapse process of a representative unit: the initial configuration (a), the idealized collapsed state (b) and densification state (c).

As shown in Figure 12, the relative displacement along the compression direction within the representative unit can be calculated as the structure transitions from the initial state (with a height of h) to the densification state (with a height of H_d), with expression of

$$\Delta u = h - H_d = h - 2t_1 - 4r_1\left(1 - \cos\theta\right) \tag{8}$$

Where t_1 is the inclined arc wall thickness and r_1 denotes the radius of inclined arc segment. Based on the principle of energy absorption conservation, the external work done by the crushing load is equal to the plastic energy dissipated. Consequently, the energy conservation equation can be written as

$$l_0 b\sigma_{\text{pl}}\Delta u = 16M_{p1}\Delta\varphi_1 + 4M_{p2}\Delta\varphi_2 + 4M_{p2}\Delta\varphi_3 \tag{9}$$

Where σ_{pl} is the plateau crushing stress, M_{p1} and M_{p2} are the fully plastic moments of cell wall of thicknesses of t_1 and t_2 with expressions of

$$M_{p1} = \frac{\sigma_y b t_1^2}{4},\ M_{p2} = \frac{\sigma_y b t_2^2}{4} \tag{10}$$

Where t_2 is the reinforced circular wall thickness, b is the thickness of structure in out-of-plane direction and σ_y is the yield stress of cell wall material. By substituting Equations (7-8, 10)))) into Equation (9), the plateau stress of CRRAH under quasi-static in-plane compression is determined as

$$\sigma_{pl} = \frac{32\sigma_y t_1^2 \theta + \pi\sigma_y t_2^2 + 5\pi\sigma_y t_2^2}{8l_0\left(h - 2t_1 - 4r_1\left(1-\cos\theta\right)\right)} \tag{11}$$

The theoretical predictions of the plateau stress for CRRAHs with γ = 0 and γ = 1 are 0.163 MPa and 0.295 MPa (i.e., the crushing forces of 0.163kN and 0.295 kN, respectively), respectively, while the corresponding numerical results are 0.149 MPa and 0.276 MPa. The relative errors between the theoretical and numerical values are 9.4% and 6.9%, respectively, as illustrated in Figure 10(a), demonstrating the accuracy of the proposed theoretical formulation in evaluating the crushing strength of CRRAHs.

3.4 Comparison of crushing performance with other types of cell configurations

To illustrate the crushing properties of the CRRAH structure, honeycombs with various typical cell configurations, namely, traditional hexagonal cell, re-entrant cell, curved cell (Feng et al., 2021), circular re-entrant cell and circular reinforced re-entrant arched cell, are constructed and analyzed. All honeycomb structures feature an identical cell wall thickness of 0.2 mm, with aluminum alloy as the base material, whose mechanical properties are listed in Table 1. For a given cell wall thickness, the CRRAH exhibits a significantly higher crushing force than the other honeycomb configurations, as shown in Figure 13(a). This performance is attributed to the presence of the reinforced circular wall at the cell center. However, the inclusion of the reinforced components in the CRRAH reduces the available compressible space, resulting in a shorter crushing distance.

A comparison of energy absorption capacity reveals that throughout the crushing process, the CRRAH with γ= 1 outperforms other honeycomb configurations in terms of SEA, as shown in Figure 13(b). Despite the early onset of the densification state in the CRRAH, its enhanced crushing strength effectively compensates for the reduced energy dissipation caused by the shortened crushing distance. Additionally, the hexagonal honeycomb presents a higher SEA than the circular re-entrant honeycomb without reinforced walls (CRRAH of γ= 0) before a crushing strain of approximately 0.65. Beyond this strain, further compression transitions the crushing process into the second stage, where the collapsed walls are further compacted until nearly reaching the densification state. Overall, the hybrid design of incorporating re-entrant arched cell walls and circular reinforced walls significantly enhances the crushing performance and ensures a more stable deformation process.

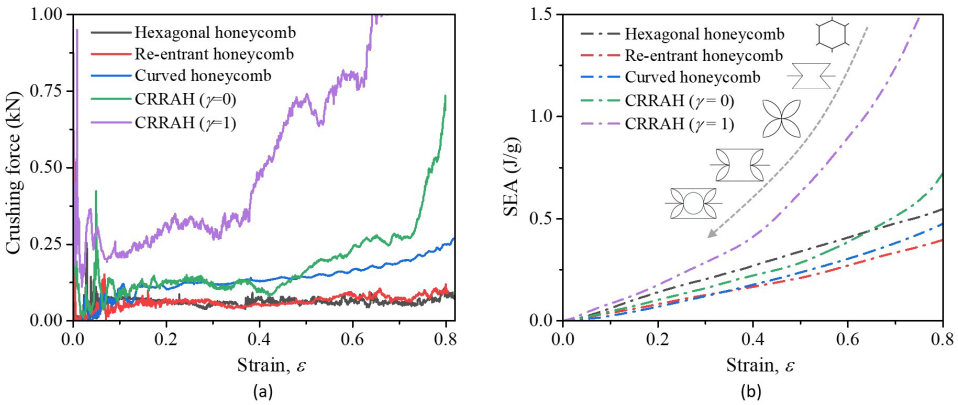

Figure 13: Comparison of the crushing responses (a) and SEA-strain curves (b) of various typical cell configurations.

3.5 Auxetic performance

Observation of the deformation patterns of CRRAH structures indicates that obvious negative Poisson's ratio (NPR) effect is presented. Essentially, the presence of NPR effect is the main reason to make the honeycomb possess enhanced shear resistance and energy absorption capacity. The NPR effect of CRRAHs is quantitatively investigated during the whole crushing process, and NPR is defined as the negative ratio of the average lateral shrinkage strain to the nominal axial strain with expression as (Hu et al., 2019)

$$\mu = -\frac{\varepsilon_x}{\varepsilon_y} = \frac{\frac{1}{LN}\sum_{i=1}^{N}\left(X_{Ai} - X_{Bi}\right)}{\delta / H} \tag{12}$$

Where L is the original width of honeycomb structure, δ is the distance of loading plate along vertically direction, X_{Ai} and X_{Bi} are the lateral Lagrange coordinates of the i-th nodes on the two free boundaries and N is the number of nodes on one free boundary, as marked in Figure 14. For the current size of CRRAH, considering the plane strain condition, the total number of nodes on the symmetrical boundary is thirteen.

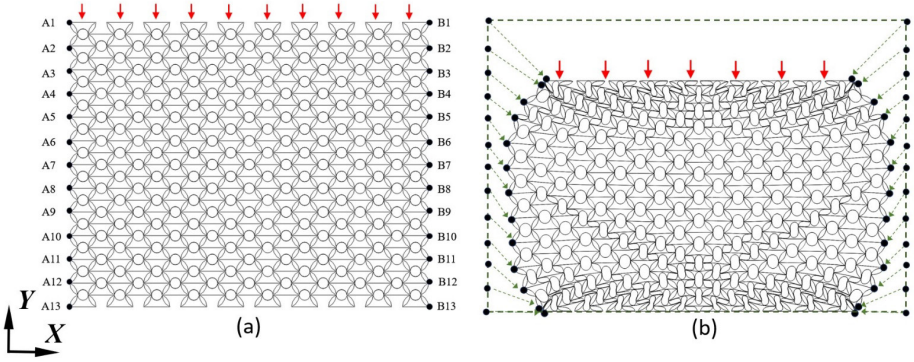

Figure 14: Positions of the targeted nodes at initial state (a) and under strain of 0.25(b).

The variation of dynamic Poisson's ratio of CRRAHs with nominal compression strain is shown in Figure 15. Both of the two types of honeycomb structures exhibit the same trend of dynamic Poisson's ratio with axial strain. At the early crushing stage, the Poisson's ratio decreases dramatically to the minimum values, and then gradually increases to constant value corresponding to the densification state. Notably, the Poisson's ratio of CRRAH of γ = 1 is initially larger than that without reinforced elements at a global axial strain of approximately 0.5. However, as the axial strain continues to increase, the Poisson's ratio of CRRAH without reinforced elements surpasses that of CRRAH of γ = 1. For CRRAH of γ = 0, the bugle effect on the free boundaries is more evident than CRRAH of γ = 1, due to the X-shaped shear band in the central site (as illustrated in Figure 9). While for CRRAH of γ = 1, the existence of reinforced components enhances the deformation stability and shear resistance, more symmetrical V-shaped shear bands formed within the structure and thus strong lateral shrinkage is induced. As the rotation and collapse of inclined edges of CRRAH of γ = 1 almost finish, the subsequent crushing of reinforced components has limited effect on the inward contraction, whereas the cells within CRRAH of γ=0 could continue shrinking until totally compaction. In this viewpoint, the introduction of reinforced component elements within re-entrant cells could influence the auxetic performance in the whole crushing process.

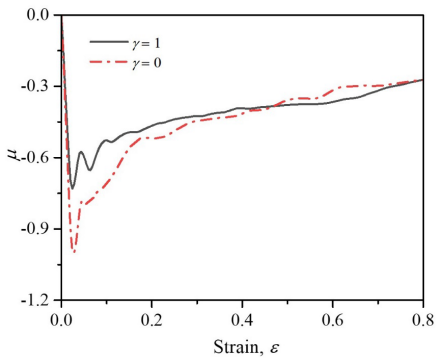

Figure 15: Variation of Poisson's ratio of CRRAHs of γ = 1 and γ = 0 with compression strain.

3.6 Effect of thickness ratio *γ* on the crushing behavior

As discussed previously, the existence of the reinforced components could affect the mesoscopic collapse evolution of cells and the macroscopic mechanical properties of CRRAH. Hereby, the relative proportion of the reinforced component within a unit cell is investigated by adopting the thickness ratio $\gamma=t_2/t_1$. Variation of SEA of CRRAH with different thickness ratios with global axial strain is shown in Figure 16(a). The SEA-ε curves for all configurations show a similar trend: an initially slow energy absorption rate at the early crushing stage that increases greatly in the later stage. When the thickness ratio $\gamma<1$, SEA of CRRAH increases significantly with increase of γ, showing a 108% increase as γ grows from 0.4 to 1 at a global strain of 0.8. However, when the thickness ratio γ exceeds 1, further increases have a very limited effect on enhancing the energy absorption performance of CRRAH. This is mainly because the continuous increase in the reinforced member wall thickness raises the overall structural mass, compromising the improvements in energy absorption capability caused by the stability-enhanced components. Therefore, in terms of energy absorption performance, simply increasing the wall thickness of the reinforced component does not always lead to effective material utilization.

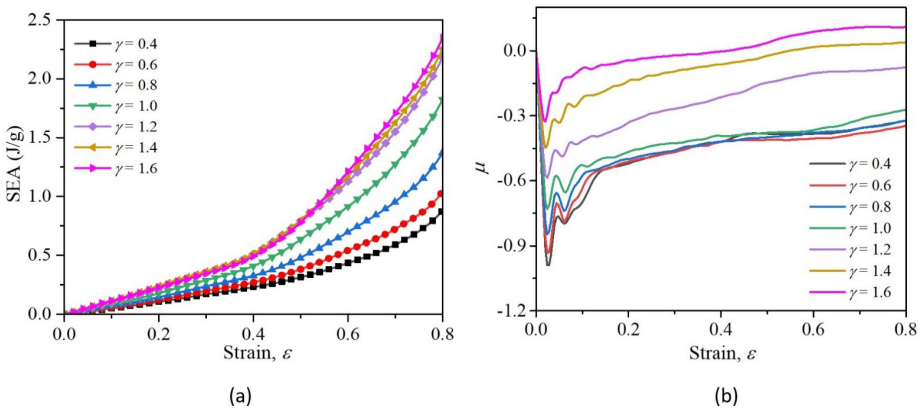

Figure 16: SEA-strain curves (a) and Poisson's ratio- strain curves (b) of CRRAHs with different thickness ratios.

Figure 16(b) shows the variation of Poisson's ratio with axial strain for CRRAHs with different thickness ratios. As mentioned above, the initial lateral contraction leads to the sharply decrease of Poisson's ratio and then generally approaches to the densification value. When the thickness ratio $\gamma<1$, the initially Poisson's ratio is largely dependent of γ, and the less of the γ value is, the less of the minimum Poisson's ratio is. For the following crushing process, the auxetic response of CRRAH with $\gamma<1$ is almost identical. However, when the thickness ratio γ is larger than 1, the thickness ratio shows significant influence on the auxetic performance of CRRAH. The large Poisson's ratio is expected to be achieved in the whole crushing process by increasing the thickness of reinforced components. It is worthy noticed that when the thickness ratio γ is increased to a certain value, the Poisson's ratio could approach to a positive value, indicating the transformation of final deformation pattern from lateral contraction to lateral expansion.

Deformation modes of CRRAHs with different thickness ratios are investigated to analyze the cell topology effect. Globally, CRRAHs with $\gamma\leq1$ exhibit lateral shrinkage shape after densification whereas that with $\gamma>1$ has slight lateral expansion after totally compacting, as shown in Figure 17. At the early stage, with axial strain of 0.25, CRRAHs of $\gamma\leq1$ crush initially at the two ends with cells in these regions shrinking inwards, forming the V-shaped crushed bands. For CRRAH of $\gamma=1$, an additional V-shaped crushed band across the lateral section prefers to firstly occur due to the relatively enhanced strength of reinforced components. With compression proceeds, more crushed bands with symmetrical distribution on both sides horizontally are formed. The collapse of cells within these deformation bands leads to the continual contraction of the disturbed regions and those on the junctions of bands are squeezed outside of structure. When the thickness ratio γ exceeds 1 (e.g., γ = 1.4), the CRRAH structure collapses in a uniform pattern rather than forming shear bands. The inclined arch edges near the loading ends are the first to undergo crushing, whereas cells in the central region maintain their shape, as shown in Figure 17(c). As the compression strain reaches 0.5, almost all the arch edges are collapsed into horizontal states whereas the reinforced components still keep undeformed states. Then, further deformation is dominated by the collapse of reinforced components, accompanying slight lateral expansion in this stage. The distinct deformation mechanisms of CRRAHs with varying thickness ratios can be explained as follows: As the thickness ratio γ increases, the difference in buckling resistance between the embedded reinforced components and inclined arch segments becomes more pronounced. This causes collapse to initiate primarily in the inclined segments, and the undeformed reinforced components thereafter inhibit the lateral contraction of the collapsed components, thereby weakening the structure's overall negative Poisson's ratio effect of CRRAH with thicker reinforced member

thickness. Consequently, by adjusting the thickness ratio *γ*, the deformation mode can shift from the initiation of localized shear bands to global compression. This transition enables the structure to better distribute compressive loads across its entirety, reducing localized stress concentrations and enhancing overall stability under loading conditions. The shift in deformation mode also contributes to more effective energy dissipation, making the structure more adaptable to being as the energy absorbing components for varying impact scenarios.

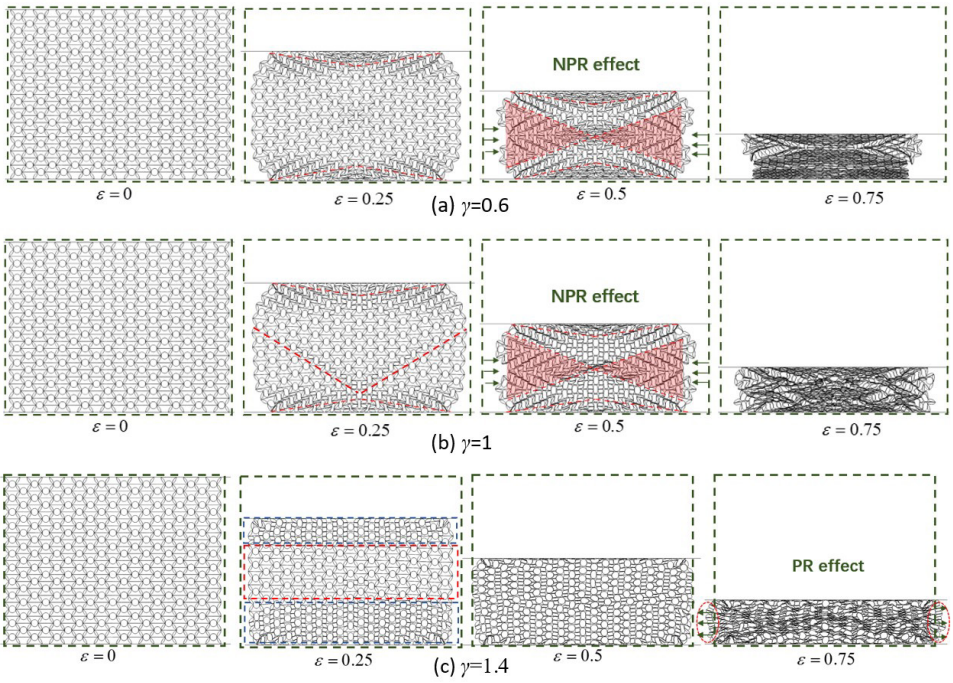

Figure 17: Deformation patterns of CRRAHs with different thickness ratios: *γ* =0.6 (a), *γ* =1 (b) and *γ* =1.4 (c).

3.7 Effect of thickness ratio *γ* on local indentation resistance

Further study is carried out to understand the effect of embedded reinforced components on the impact and indentation resistance of CRRAHs. A semi-cylindrical indenter with a diameter of 49 mm is considered and a point mass with specific value is attached on the indenter to ensure that the impact energy can be a constant of 10 J under different impact velocities. To achieve this loading condition, the masses of the indenter under the impact velocities of 20 m/s and 100m/s are 50 g and 2 g, respectively. CRRAH structures with a varying thickness ratio ranging from 0 to 1.4 are considered. It is pointed that while experimental tests on CRRAH structures under dynamic loading were not conducted, finite element models using a rate-independent aluminum alloy as the base material have been extensively employed to investigate the mechanical behavior of cellular structures under impact loading (Yang et al., 2017; Lin et al., 2023; Meng et al., 2020). In these studies, the mechanical behavior of the cellular structures was also compared with experimental results and theoretical predictions, ensuring that the reliability of the numerical models using similar base materials has been well validated.

The deformation pattern of CRRAH structures under two impact-velocity indentations is shown in Figure 18. Under moderate impact velocity of 20 m/s, the cells around the indenter are initially collapsed and the re-entrant cells within these regions shrink towards the indentation path, showing an obvious negative Poisson's ratio effect. With increase of thickness ratio *γ*, the number of cells being incorporated to collapse decreases and the contraction effect is generally weakened. Under this impact velocity, slight lateral deformation of the reinforced components in the distributed region occurs when *γ* = 1 while the lateral squeezing would be further weakened as γ increase to 1.4. Additionally, the ultimate depth of indenter (D_u) is decreased with increasing of parameter *γ*. Analysis of the responses of the impact velocity and indentation displacement indicates that the initial velocity decays more rapidly and the impact process is terminated faster for a higher value of *γ*, as shown in Figure 19(a). The inclusion of enhanced elements in CRRAH significantly improves its indentation resistance. Additionally, the large difference in wall thickness between the re-entrant cell edges and the reinforced members allows the inclined edges to undergo rotational deformation more readily around the reinforced elements. This behavior creates a strengthened zone around the indenter, which enhances structural stability and ensures high energy absorption along the indentation path.

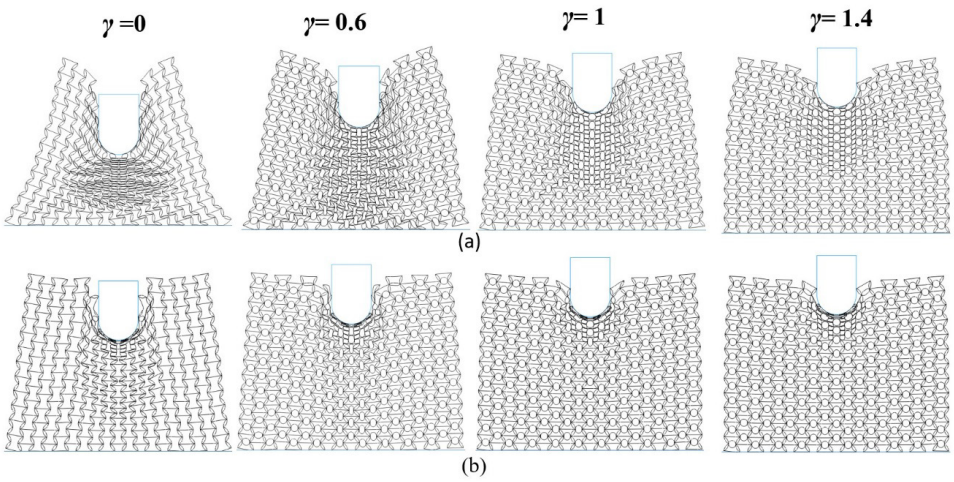

Figure 18: Deformation modes of CRRAHs at ultimate indentation depth under impact velocities of 20 m/s (a) and 100 m/s (b).

When the impact velocity is increased to 100 m/s, the collapsed cells are narrowly limited on the indentation path, as shown in Figure 18(b). With increase of parameter γ, the number of cells involved in transverse contraction is significantly reduced under high-velocity impact compared to that under relatively low-velocity impact. This is explained as the inertial effect-dominated deformation for high impact intensity (Wei et al., 2020). Figure 19(b) demonstrates that variations in the thickness of reinforced elements have slight effect on velocity attenuation until the impact velocity drops to approximately 40 m/s. When the impact velocity decreases below 40 m/s, CRRAH with a higher parameter *γ* dissipates the residual energy more effectively, resulting in a smaller ultimate indentation depth. Additionally, for a given *γ*, the ultimate indentation depth D_u is observed to be smaller under high-velocity impacts compared to CRRAH at lower velocities (e.g., *V*=20m/s). This is because, under high-velocity impacts, cell collapse occurs in a highly localized region near the indenter, whereas at lower velocities, deformation is distributed over a broader area along the loading path. Overall, incorporating reinforced elements into re-entrant cells significantly improves the indentation resistance of re-entrant honeycombs by reducing indentation depth and enhancing external kinematic energy attenuation. It is worth pointing that the indentation resistance of the developed CRRAH could be effectively utilized when incorporated as the core member in a composite sandwich structure. In such a structure, the lightweight CRRAH core separates the face skins, significantly increasing the bending stiffness with small weight addition. For a sandwich structure with a CRRAH core, horizontal shrinkage deformation occurs under transverse compression or impact, leading to material concentration in the localized regions of the CRRAH core (as discussed in the deformation mechanism above). This behavior further enhances the superior indentation resistance and impact energy absorption, offering superior performance compared to traditional honeycomb structures.

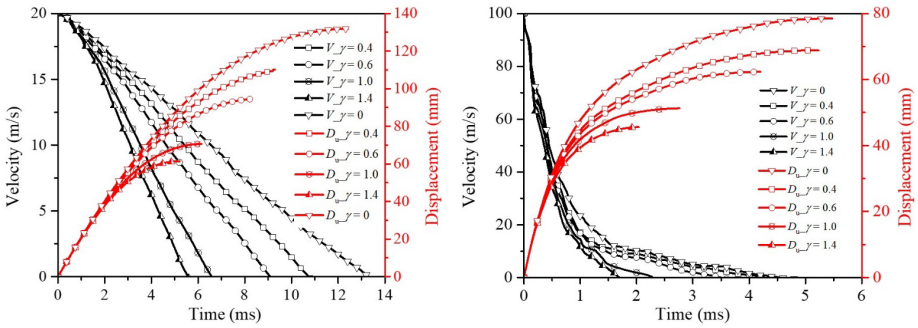

Figure 19: Variation of velocity-time and indentation depth-time responses of CRRAHs with varying *γ* under impact velocities of *V* = 20 m/s (a) and *V* = 100 m/s (b).

4 CONCLUSION

By hybridizing an arched re-entrant unit with a circular reinforced rib, a novel circular reinforced re-entrant arched honeycomb (CRRAH) structure was designed to improve the deformation stability and energy absorption performance.

The in-plane crushing behavior of the developed CRRAH was investigated both experimentally and numerically. The underlying deformation and enhancement mechanisms were also revealed. Additionally, the effect of thickness ratio of the reinforced circular rib to the re-entrant edges on the crushing properties, including deformation mode, crushing strength, energy absorption capacity, and indentation resistance, was explored.

The crushing strength and the energy absorption capacity of CRRAH structure are significantly improved while maintaining considerable auxetic behavior by embedding the circular rib into re-entrant cell. A 208% increase in the SEA is demonstrated when comparing the energy absorption capacity of the additively manufactured ABS CRRAH structure to that of the arched re-entrant honeycomb. Additionally, the CRRAH structure exhibits a two-stage response within the plateau region: an initial stage characterized by a nearly constant crushing force stage, where deformation is primarily governed by inclined arched ligaments, followed by an extended hardening phase dominated by the collapse of reinforced circular ribs.

As the thickness ratio γ increases, the deformation behavior of the CRRAH structure shifts from a V-shaped localized shear band formation with inward contraction to a mode of globally uniform compression accompanied by lateral expansion. For thickness ratios where $\gamma > 1$, increasing the wall thickness of the reinforced circular rib has limited contribution on improving SEA, yet significantly affects the auxetic behavior. Conversely, when $\gamma < 1$, increasing reinforced circular ribs' thickness effectively enhances SEA, with only a slight influence on the dynamic Passion's ratio.

The developed CRRAH structure exhibits superior indentation resistance under different impact velocity intensities compared to arched re-entrant honeycomb structures. With increase of thickness ratio, the collapse of cells becomes more localized to a narrow region ahead of indenter, leading to an enhanced indentation resistance along the loading path. A higher thickness ratio results in a shortened impact process and reduced indentation depth.

The design concept of the CRRAH, which incorporates the tailored deformation mechanism with additive manufacturing technique, offers valuable insights for engineering applications of lightweight structures with enhanced performance and sustainable materials. In future studies, CRRAH-based composite structures may be explored under different loading scenarios and design objectives to further optimize their performance and expand their application potential.

Acknowledgments

The current work reported herein is supported by the Natural Science Foundation-funded by the Department of Education, Anhui Province, China (No. 2023AH051083).

Author's Contributions: Conceptualization, SL Wang; Writing - original draft, SL Wang and Y Liu; Methodology, SL Wang and HY Bao; Investigation, Y Liu and ZL Huang; Formal analysis, SL Wang, Y Liu and HY Bao; Writing - review & editing, HY Bao; Funding acquisition, SL Wang; Resources, Y Liu and ZL Huang.

Editor: Rogério José Marczak

References

Arnob, F. F., Anwar, M. S., Islam, M. S., Arifuzzaman, M., Bari, M. A. A., (2023). Negative stiffness honeycomb structure as automobile leaf spring: A numerical investigation. Engineering Solid Mechanics, 11(4), 389-400.

Azam, M. U., Schiffer, A., Kumar, S. (2023). Piezoresistive behavior of MWCNT/PA12 honeycomb composites processed via selective laser sintering. Journal of Materials Research and Technology, 26, 2319-2332.

Baran, T., Öztürk, M., (2020). In-plane elasticity of a strengthened re-entrant honeycomb cell. European Journal of Mechanics-A/Solids, 83, 104037.

Bohara, R. P., Linforth, S., Nguyen, T., Ghazlan, A., Ngo, T., (2023). Anti-blast and-impact performances of auxetic structures: A review of structures, materials, methods, and fabrications. Engineering Structures, 276, 115377.

Chen, G., Zhang, P., Liu, J., Cheng, Y., Wang, H. (2019). Experimental and numerical analyses on the dynamic response of aluminum foam core sandwich panels subjected to localized air blast loading. Marine Structures, 65, 343-361.

Chen, Y., Fu, M. H., (2018). Design and modeling of a combined embedded enhanced honeycomb with tunable mechanical properties. Applied Composite Materials, 25(5), 1041-1055.

Chen, Z., Li, J., Wu, B., Chen, X., Xie, Y. M., (2024). Enhanced mechanical properties of re-entrant auxetic honeycomb with self-similar inclusion. Composite Structures, 331, 117921.

Deshmukh, D., Kulkarni, H., Srivats, D. S., Bhanushali, S., More, A. P. (2024). Recycling of acrylonitrile butadiene styrene (ABS): a review. Polymer Bulletin, 1-38.

Feng, G., Li, S., Xiao, L., Song, W., (2021). Energy absorption performance of honeycombs with curved cell walls under quasi-static compression. International Journal of Mechanical Sciences, 210, 106746.

Feng, X., Wang, B., Wu, X., Wang, X., Guo, Y., (2023). In-plane compression behavior of sinusoidal honeycomb with circular nodes. Chinese Journal of Theoretical and Applied Mechanics, 55(9), 1910-1920.

Fu, M. H., Chen, Y., Hu, L. L., (2017). A novel auxetic honeycomb with enhanced in-plane stiffness and buckling strength. Composite Structures, 160, 574-585.

Garbatov, Y., Marchese, S. S., Epasto, G., Crupi, V. (2024). Flexural response of additive-manufactured honeycomb sandwiches for marine structural applications. Ocean Engineering, 302, 117732.

Giménez-Ribes, G., van der Linden, E., Habibi, M., (2022). Auxetic behavior and unusual shear resistance of crumpled materials: Opportunities for programming the nonlinear responses of crumpled mechanical metamaterials. Materials & Design, 223, 111258.

Guo, Z., Li, Z., Lin, J., Mo, Z., Li, J., (2023). Multi-scale characterization and in-plane crushing behavior of the elliptical anti-chiral honeycomb. Composite Structures, 303, 116345.

Hu, L. L., Luo, Z. R., Yin, Q. Y., (2019). Negative Poisson's ratio effect of re-entrant anti-trichiral honeycombs under large deformation. Thin-Walled Structures, 141, 283-292.

Isaac, C. W., Duddeck, F. (2022). Current trends in additively manufactured (3D printed) energy absorbing structures for crashworthiness application–a review. Virtual and Physical Prototyping, 17(4), 1058-1101.

Jafari Nedoushan, R., An, Y., Yu, W. R., (2023). New auxetic materials with stretch-dominant architecture using simple trusses. Mechanics of Advanced Materials and Structures, 30(3), 609-625.

Joseph, T. M., Kallingal, A., Suresh, A. M., Mahapatra, D. K., Hasanin, M. S., Haponiuk, J., Thomas, S. (2023). 3D printing of polylactic acid: recent advances and opportunities. The International Journal of Advanced Manufacturing Technology, 125(3), 1015-1035.

Körner, C., Liebold-Ribeiro, Y., (2014). A systematic approach to identify cellular auxetic materials. Smart Materials and Structures, 24(2), 025013.

Li, R., Zhao, Z., Bao, H., Pan, Y., Wang, G., Liu, B., Liao, T., Li, J., (2024). Bio-inspired honeycomb structures to improve the crashworthiness of a battery-pack system. Engineering Failure Analysis, 158, 108041.

Li, T., Liu, F., Wang, L., (2020). Enhancing indentation and impact resistance in auxetic composite materials. Composites Part B: Engineering, 198, 108229.

Li, X., Wang, Q., Yang, Z., Lu, Z., (2019). Novel auxetic structures with enhanced mechanical properties. Extreme Mechanics Letters, 27, 59-65.

Lin, S., Yuan, M., Zhao, B., Li, B. (2023). Out-of-plane compression behaviour of aluminum alloy large-scale super-stub honeycomb cellular structures. Materials, 16(3), 1241.

Meng, Y., Lin, Y., Zhang, Y., Li, X. (2020). Study on the dynamic response of combined honeycomb structure under blast loading. Thin-Walled Structures, 157, 107082.

Ni, X. H., Teng, X. C., Jiang, W., Zhang, Y., Ren, X., (2024). Multi-objective optimization and theoretical analysis of re-entrant structure with enhanced mechanical properties. Thin-Walled Structures, 199, 111791.

Nunes, J. P., Silva, J. F. (2016). Sandwiched composites in aerospace engineering. Advanced Composite Materials for Aerospace Engineering. Woodhead Publishing.

Olivera, S., Muralidhara, H. B., Venkatesh, K., Gopalakrishna, K., Vivek, C. S. (2016). Plating on acrylonitrile–butadiene–styrene (ABS) plastic: a review. Journal of materials science, 51, 3657-3674.

P.R. China, Standardization Administration, State Administration for Market Regulation (2018). Plastics—Determination of Tensile Properties—Part 1: General Principles [standard], China Standard Press.

Palomba, G., Epasto, G., Sutherland, L., Crupi, V. (2022). Aluminium honeycomb sandwich as a design alternative for lightweight marine structures. Ships and Offshore Structures, 17(10), 2355-2366.

Pang, L., Ma, Y., Song, X., Wang, H., Wang, L., Peng, W., Wan, Y., Feng, R., (2024). Experimental and simulation study on effects of material and loading direction on the quasi-static compression behavior of re-entrant honeycomb structure. Materials Today Communications, 39, 109005.

Qi, C., Jiang, F., Remennikov, A., Pei, L. Z., Liu, J., Wang, J. S., Liao, X.-W., & Yang, S., (2020). Quasi-static crushing behavior of novel re-entrant circular auxetic honeycombs. Composites Part B: Engineering, 197, 108117.

Qi, C., Jiang, F., Yang, S., (2021). Advanced honeycomb designs for improving mechanical properties: A review. Composites Part B: Engineering, 227, 109393.

Ran, C., Yang, B., (2020). Plastic deformation and mixed-mode I/II fracture behavior of un-plasticized polyvinyl chloride. Engineering Fracture Mechanics, 230, 106973.

Ren, X., Das, R., Tran, P., Ngo, T. D., Xie, Y. M., (2018). Auxetic metamaterials and structures: a review. Smart materials and structures, 27(2), 023001.

Rezaeian, P., Ayatollahi, M. R., Nabavi-Kivi, A., Razavi, N., (2022). Effect of printing speed on tensile and fracture behavior of ABS specimens produced by fused deposition modeling. Engineering Fracture Mechanics, 266, 108393.

Shen, L., Wang, Z., Wang, X., Wei, K., (2021). Negative Poisson's ratio and effective Young's modulus of a vertex-based hierarchical re-entrant honeycomb structure. International Journal of Mechanical Sciences, 206, 106611.

Tatlıer, M. S., Öztürk, M., Baran, T., (2021). Linear and non-linear in-plane behaviour of a modified re-entrant core cell. Engineering Structures, 234, 111984.

Wang, Z., (2019). Recent advances in novel metallic honeycomb structure. Composites Part B: Engineering, 166, 731-741.

Wang, H., Lu, Z., Yang, Z., Li, X., (2019). A novel re-entrant auxetic honeycomb with enhanced in-plane impact resistance. Composite Structures, 208, 758-770.

Wang, S., Zhang, M., Wang, Y., Huang, Z., Fang, Y., (2021). Experimental studies on quasi-static axial crushing of additively-manufactured PLA random honeycomb-filled double circular tubes. Composite Structures, 261, 113553.

Wang, S., Liu, H. T., Cai, G. B., (2024a). Programmable mechanical responses of a hybrid star-rhombus honeycomb based on digital design method. Thin-Walled Structures, 205, 112399.

Wang, S., Pei, W., Jin, S., Yu, H., (2024b). Numerical and theoretical analysis of the out-of-plane crushing behavior of a sinusoidal-shaped honeycomb structure with tunable mechanical properties. Structures, 61, 106147.

Wei, L., Zhao, X., Yu, Q., Zhu, G., (2020). A novel star auxetic honeycomb with enhanced in-plane crushing strength. Thin-Walled Structures, 149, 106623.

Xiao, D., Dong, Z., Li, Y., Wu, W., Fang, D., (2019). Compression behavior of the graded metallic auxetic reentrant honeycomb: Experiment and finite element analysis. Materials Science and Engineering: A, 758, 163-171.

Xu, M., Xu, Z., Zhang, Z., Lei, H., Bai, Y., Fang, D., (2019). Mechanical properties and energy absorption capability of AuxHex structure under in-plane compression: Theoretical and experimental studies. International Journal of Mechanical Sciences, 159, 43-57.

Yang, J., Wang, S., Ding, Y., Zheng, Z., Yu, J. (2017). Crashworthiness of graded cellular materials: A design strategy based on a nonlinear plastic shock model. Materials Science and Engineering: A, 680, 411-420.

Zhang, W., Xu, J., (2022). Advanced lightweight materials for Automobiles: A review. Materials & Design, 221, 110994.

Zhang, X. C., An, C. C., Shen, Z. F., Wu, H. X., Yang, W. G., Bai, J. P., (2020). Dynamic crushing responses of bio-inspired re-entrant auxetic honeycombs under in-plane impact loading. Materials Today Communications, 23, 100918.

Zhang, X. Y., Ren, X., Zhang, Y., Xie, Y. M., (2022a). A novel auxetic metamaterial with enhanced mechanical properties and tunable auxeticity. Thin-Walled Structures, 174, 109162.

Zhang, X., Hao, H., Tian, R., Xue, Q., Guan, H., Yang, X., (2022b). Quasi-static compression and dynamic crushing behaviors of novel hybrid re-entrant auxetic metamaterials with enhanced energy-absorption. Composite Structures, 288, 115399.

Zhao, J., Cui, Z., Wang, S., Sun, Z., Ding, Y. (2024). Flexural response of additively manufactured honeycomb sandwich structures with continuous density-gradient variations. Thin-Walled Structures, 197, 111642.

Zheng, Z., Yu, J., Li, J., (2005). Dynamic crushing of 2D cellular structures: A finite element study. International journal of impact engineering, 32(1-4), 650-664.

Zhu, D., Wei, Y., Shen, X., Yan, K., Yuan, M., Qi, S., (2024). A novel elliptical annular re-entrant auxetic honeycomb with enhanced stiffness. International Journal of Mechanical Sciences, 262, 108732.

Zou, Z., Xu, F., Niu, X., Fang, T., Jiang, Z., (2023). In-plane crashing behavior and energy absorption of re-entrant honeycomb reinforced by arched ribs. Composite Structures, 325, 117615.